

Porous Co₃O₄/Si Composite Film with Interconnected Network Structure as Anode for Lithium-Ion Batteries

X. H. Huang*, J. B. Wu, Y. Q. Cao, Y. Lin, W.W. Zhong

Department of Materials Engineering, Taizhou University, Taizhou 318000, China

*E-mail: huangxh@tzc.edu.cn

Received: 31 September 2018 / Accepted: 19 November 2018 / Published: 5 January 2019

Well-designed nanostructured composites are of great importance in the research field of electrode materials for lithium-ion batteries, because they can solve the problems of lithium-ion diffusion, electron transport and particle pulverization. In this work, a porous Co₃O₄/Si nanocomposite film with interconnected network structure, assembled by nanosheets growing perpendicular to the substrate, is designed and prepared as anode materials for lithium-ion batteries. The composite film is fabricated using chemical bath deposition plus radio-frequency magnetron sputtering. The film is characterized by means of scanning electron microscopy (SEM), transmission electron microscopy (TEM) and energy dispersive spectrometry (EDS). The electrochemical performance as lithium-ion anode materials is investigated by galvanostatic discharge-charge cycling and cyclic voltammetry (CV). The Co₃O₄/Si film delivers significantly enhanced electrochemical performance than the pure Co₃O₄ film. The enhancement is ascribed to the Si component in the composite, the interconnected network structure of the film, and the Si-coated Co₃O₄ structure of the nanosheet.

Keywords: Cobalt oxide; Silicon; Nanostructure; Anode materials; Lithium ion battery

1. INTRODUCTION

Co₃O₄, a typical 3d transition-metal oxide, is a frequently studied material for energy storage and conversion. In the field of lithium-ion batteries, Co₃O₄ is used as anode materials based on the mechanism of reversible conversion reaction and its theoretical specific capacity is as high as 890 mAh g⁻¹. However, because of the drawbacks of low conductivity and pulverization of active particles, the actual reversible capacity may be much lower, especially at high discharge/charge current densities, and often reduces quickly during the cycling process [1–3]. Preparing nanostructured composite by introducing metals and/or carbon, both of which have high conductivity and ductility, is the most common approach to improve the rate capability and cycling stability [4–8]. These components undoubtedly reduce the overall specific mass capacity of the composite due to their lithium-inactive or

low-capacity nature. To overcome this problem, it is naturally to think of that forming composite with higher-capacity components should be an effective way. It is well known that Si is such a material, whose theoretical capacity is as high as 4200 mAh g^{-1} . Although the unmodified Si materials always show poor rate capability and cycling stability due to the low conductivity and high brittleness [9–14], they still can achieve improved performance by the method of fabricating nanostructured composite [15, 16]. In the past decade, various nanostructures, such as porous [17], hollow [18], spherical [19], core@shell [20], et. al, have been designed and applied successfully [21]. Therefore, it is possible for the composite prepared by introducing Si into Co_3O_4 to get both increased specific capacity and enhanced cycling performance if its nanostructure is well designed.

Based on above analysis, in this present work, $\text{Co}_3\text{O}_4/\text{Si}$ nanocomposite film is designed into an interconnected network structure, and the electrochemical performance as anode for lithium-ion batteries is investigated in detail.

2. EXPERIMENTAL

$\text{Co}_3\text{O}_4/\text{Si}$ film was prepared by a two-step procedure. The first step was the preparation of Co_3O_4 film by chemical bath deposition method. Briefly, 100 mL aqueous solution containing 0.4 mol L^{-1} CoSO_4 and 0.075 mol L^{-1} $\text{K}_2\text{S}_2\text{O}_8$, was used as the bath solution. A nickel foil substrate, one side covered by PTFE tape, was suspended vertically in the solution. The deposition was initiated by injecting 10 mL concentrated ammonia ($\text{NH}_3 \cdot \text{H}_2\text{O}$, 25 wt.%) and proceeded for 1 h under mild stirring at room temperature. The obtained precursor film was washed with distilled water for several times, dried in air, and calcined in a quartz-tube furnace at $350 \text{ }^\circ\text{C}$ for 1 h under flowing argon. The subsequent step was the further deposition of Si onto the Co_3O_4 film by radio-frequency magnetron sputtering technique (DE500, DE Technology, Beijing). A polycrystalline Si wafer (99.9999%), 6 cm in diameter, was used as the target, and it was fixed at 20 cm above the substrate holder. After the chamber was pumped to a base pressure of $0.5 \text{ } \mu\text{Torr}$, high purity argon (99.999%) was introduced as the working gas and its pressure was maintained at 8 mTorr. Under the radio frequency power of 60 W, the magnetron sputtering proceeded for 5, 10, 15, 20, 25 and 30 min, respectively, to obtain a set of composite films with increasing Si content. When the sputtering process was finished, the samples remained in the vacuum chamber and finally they were heat treated at $450 \text{ }^\circ\text{C}$ for 3 h.

The films were characterized by means of scanning electron microscopy (SEM, Hitachi S4800), transmission electron microscopy (TEM, FEI Tecnai G2 F20) and energy dispersive spectroscopy (EDS). The mass of active materials in the films was determined by the high-precision balance equipped in a simultaneous thermal analyzer (Netzsch, STA 449 F3).

CR2025 coin-type cells were used to investigate the electrochemical performance of the films. The cells were assembled in an argon-filled glove box (Mikrouna Super), using the films as working electrodes, Li foil as counter electrodes, and Celgard 2400 membrane as separators. The electrolyte was 1 mol L^{-1} LiPF_6 in a mixture of ethylene carbonate (EC) and dimethyl carbonate (DMC) (1:1 V/V). The cells were discharge-charged for 100 cycles on a battery test system (LAND CT2001A) using different

constant current densities between two cut-off potentials of 0.005 and 3 V. Cyclic voltammetry (CV) analysis of the cells was conducted on an electrochemical workstation (Autolab PGSTAT302N).

3. RESULTS AND DISCUSSION

The mass of the Co_3O_4 and Si component in the composite films are determined by the weight increments before and after the deposition or sputtering processes. For the Co_3O_4 film, it is calculated that the areal density is 0.15 mg cm^{-2} .

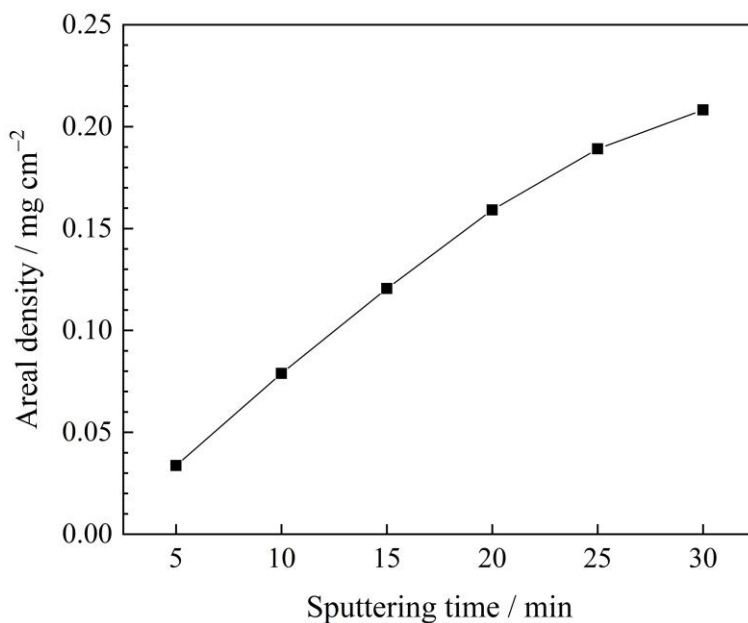
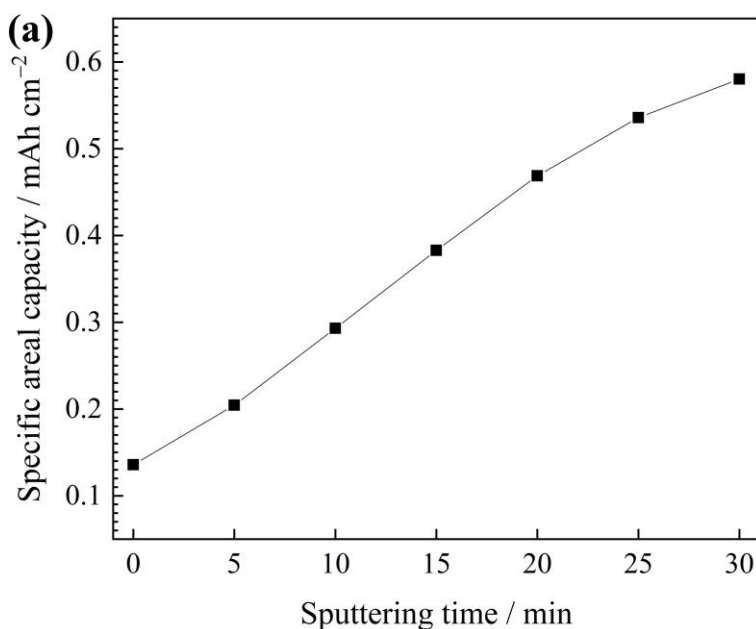


Figure 1. The evolution of Si areal density in the film with the sputtering time.



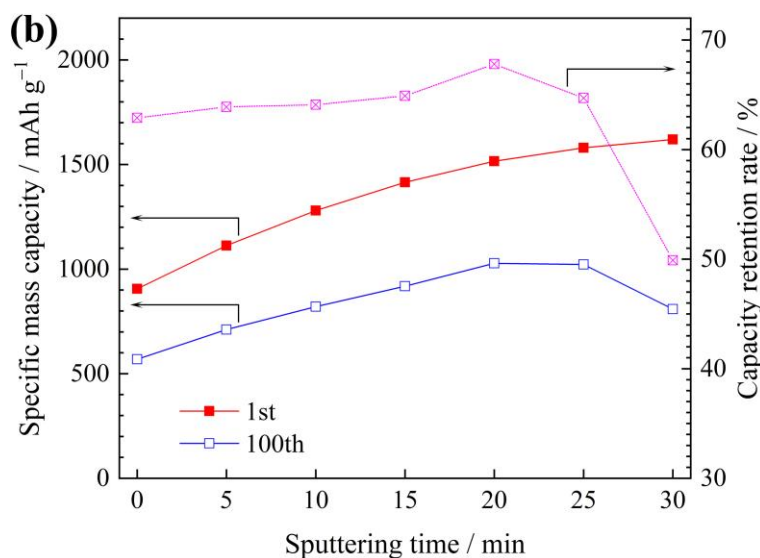


Figure 2. Comparison of (a) specific areal capacities, (b) specific mass capacities and capacity retention rates of the samples tested at the current density of 50 mA g^{-1} .

For the $\text{Co}_3\text{O}_4/\text{Si}$ composite films, the areal density of Si component increases gradually with the sputtering time, as shown in Figure 1. All the films have sub-milligrams of active materials, so they can deliver higher specific areal capacities and are more likely to meet the demands of practical applications.

As anode materials for lithium ion batteries, all the Co_3O_4 and $\text{Co}_3\text{O}_4/\text{Si}$ films are firstly tested by galvanostatic discharge-charge for 100 cycles between two cut-off potentials of 0.005 and 3 V at the constant current density of 50 mA g^{-1} , and their capacities are compared in Figure 2. The first specific areal capacities (charge capacities) of these films are compared in Figure 2a. The capacity increases significantly with the sputtering time of Si, and the value can be as high as about 0.5 mAh cm^{-2} for the samples with high Si content. Their specific mass capacities are compared in Figure 2b, which shows the variation of the first charge capacity, the 100th charge capacity, and the capacity retention rate with the sputtering time. The initial capacity increases with the sputtering time due to the increasing content of Si. After 100 cycles, they show different cycling stability. The capacity retention rate increases at first, but finally decreases dramatically. It is reasonable to believe that the sample subjected to 20 min sputtering of Si, in which the areal density of Si is 0.16 mg cm^{-2} , has the best performance, as it delivers significantly increased specific capacity, and shows the most stable cyclability. Therefore, this sample is further characterized and analyzed specially.

Figure 3 compares the SEM images of the films before and after the sputtering of Si for 20 min. The Co_3O_4 film (Figure 3a) is highly porous, showing an interconnected network structure, which is assembled by nanosheets almost perpendicular to the substrate. After the sputtering of Si (Figure 3b), the interconnected network structure is still preserved, but the thickness of nanosheets increases due to the surface coating of Si layer. The inserted cross-sectional image indicates that the vertically growing nanosheets have a height of about $1 \mu\text{m}$.

Figure 4 compares the TEM results of the two samples. The TEM image of Co_3O_4 nanosheets (Figure 4a) shows some wrinkling on the edge due to its ultrathin thickness. The surface of the nanosheets is very clean and there are no attached particles. The corresponding SAED pattern exhibits

diffraction rings that can be well indexed to the atomic planes of Co_3O_4 , indicative of its polycrystalline nature. Figure 4b is the TEM image of a $\text{Co}_3\text{O}_4/\text{Si}$ nanosheet. It shows many additional well-dispersed nanoparticles attached on the nanosheets, and they are further analyzed by means of HRTEM and EDS. The HRTEM image reveals a spacing of atomic planes of 0.31 nm, which corresponds to that of the (111) planes of Si. The EDS pattern is given in Figure 4c. Apart from the peaks originated from Co_3O_4 nanosheet and copper grid holder, the pattern shows strong peaks of Si. Therefore, it can be concluded that these nanoparticles are crystalline Si.

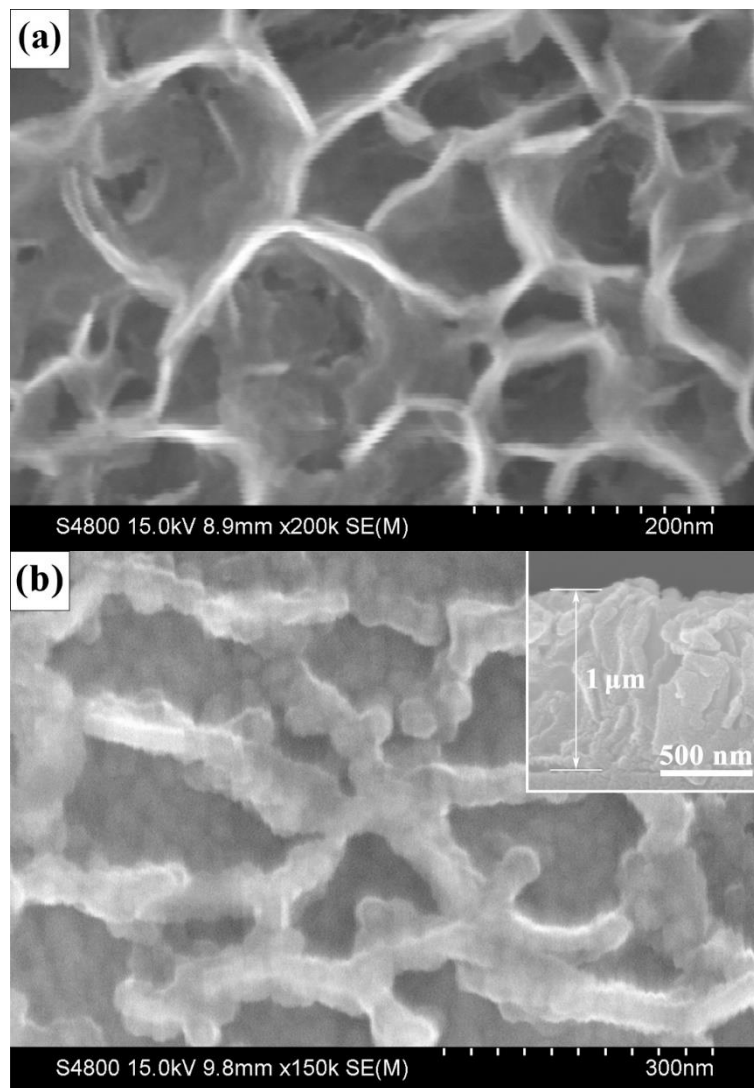


Figure 3. SEM images of the (a) Co_3O_4 film and (b) $\text{Co}_3\text{O}_4/\text{Si}$ film subjected to 20 min sputtering. The insertion is the cross-sectional image.

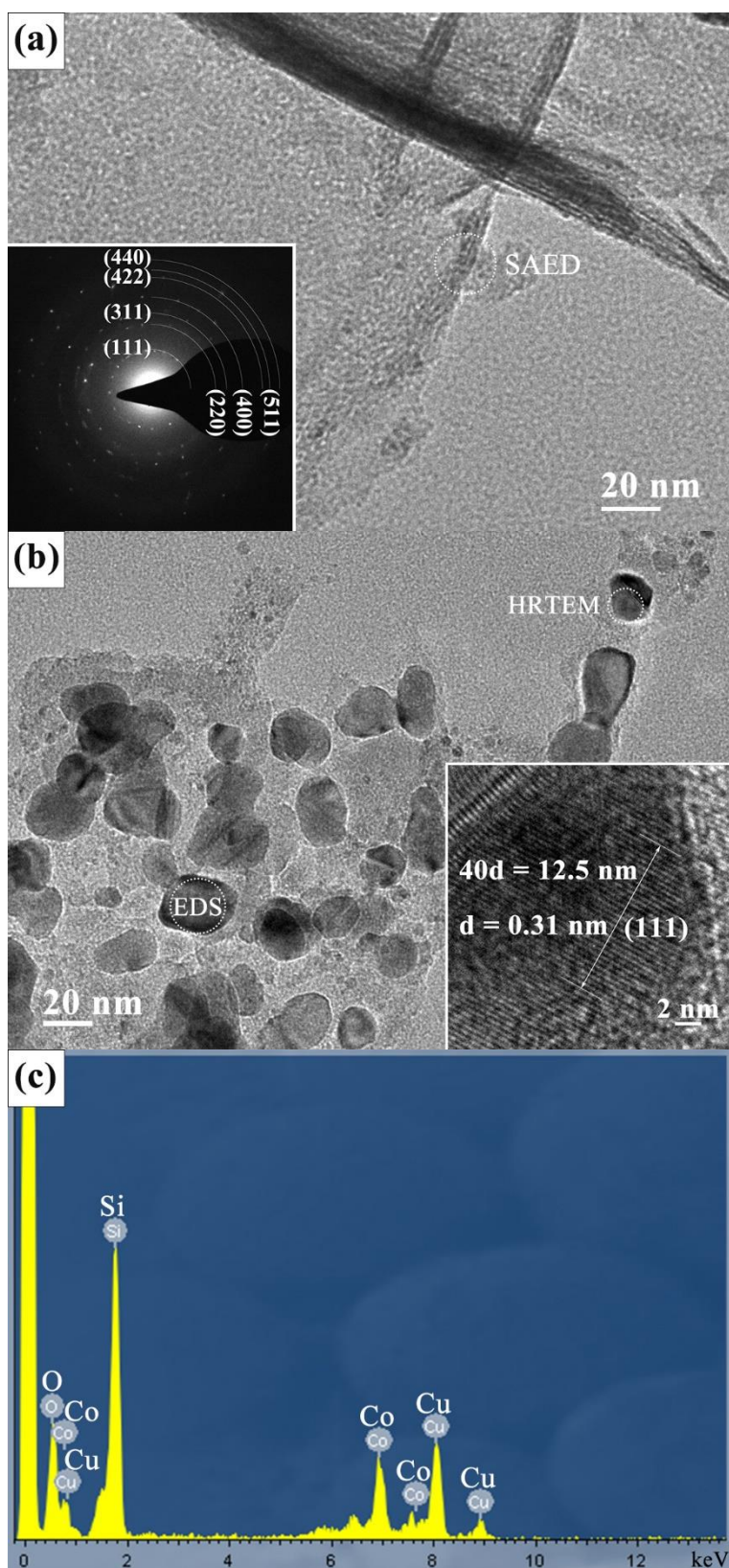


Figure 4. TEM results of the samples. (a) TEM image of Co_3O_4 nanosheets and the corresponding SAED pattern. (b) TEM image of a $\text{Co}_3\text{O}_4/\text{Si}$ nanosheet and the HRTEM image of a nanoparticle. (c) EDS pattern of a nanoparticle.

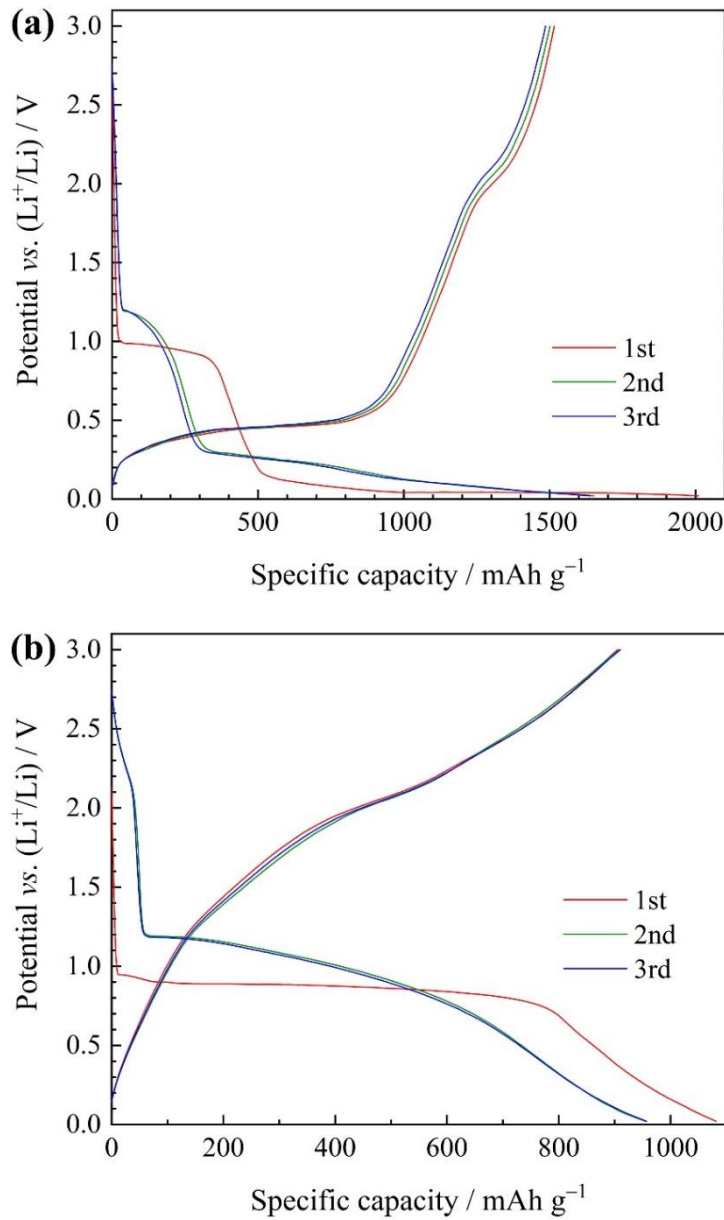


Figure 5. Discharge–charge curves of the (a) $\text{Co}_3\text{O}_4/\text{Si}$ and (b) Co_3O_4 film electrodes at the current density of 50 mA g^{-1} between 0.005 and 3 V.

Table 1. Comparison of initial reversible capacities and capacity increments relative to pristine Co_3O_4 of different Co_3O_4 -based anode materials reported in literature and those in this work.

Materials	Initial reversible capacities (mAh g^{-1})	The capacity increments (mAh g^{-1})	References
$\text{Co}_3\text{O}_4/\text{Sn}$	872	252	[22]
$\text{Co}_3\text{O}_4/\text{Fe}_3\text{O}_4$	1138	256	[23]
$\text{Co}_3\text{O}_4/\text{Fe}_2\text{O}_3$	1310	510	[24]
$\text{Co}_3\text{O}_4/\text{ZnO}$	1164	/	[25]
$\text{Co}_3\text{O}_4/\text{MnO}_2$	1220	457	[26]
$\text{Co}_3\text{O}_4/\text{Si}$	1516	611	this work

Figure 5 shows the galvanostatic discharge-charge curves of the two film electrodes between 0.005 and 3 V at 50 mA g^{-1} . From the comparison it can be inferred that the $\text{Co}_3\text{O}_4/\text{Si}$ film electrode shows the characteristic plateaus of both Co_3O_4 and Si. Both curves display discharge plateaus around 1.0 V and charge plateaus around 2.0 V, which are related to the lithiation and delithiation processes of Co_3O_4 , respectively. The other plateaus in the curve of $\text{Co}_3\text{O}_4/\text{Si}$ film, i.e., the discharge plateaus below 0.3 V and the charge plateaus below 0.5 V, are attributed to the typical alloying and dealloying reactions between Li and Si, respectively [9–11]. The initial reversible capacity (charge capacity) of $\text{Co}_3\text{O}_4/\text{Si}$ film is 1516 mAh g^{-1} , much higher than that of Co_3O_4 film (905 mAh g^{-1}). The increment is as high as 611 mAh g^{-1} , much greater than those arising from other lithium-active components also having higher capacities, for example, Sn, Fe_3O_4 , Fe_2O_3 , ZnO and MnO_2 , as listed in Table 1. This confirms that forming composite with Si is more effective for the improvements of specific capacities.

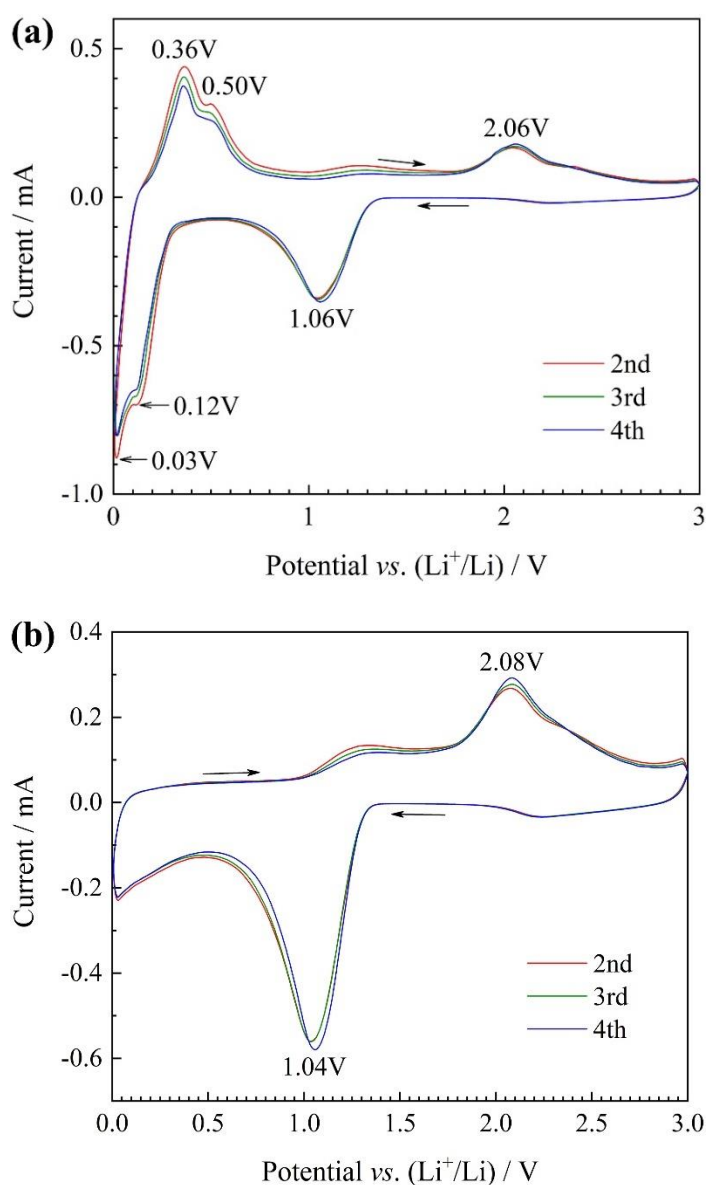


Figure 6. CV curves of the (a) $\text{Co}_3\text{O}_4/\text{Si}$ and (b) Co_3O_4 film electrodes at a scan rate of 0.05 mV s^{-1} between 0 and 3 V.

Figure 6 compares the CV curves of the two film electrodes obtained at a scan rate of 0.05 mV s^{-1} between 0 and 3 V. The potentials of cathodic/anodic peaks are well in accordance with those of discharge/charge plateaus in discharge-charge curves. The $\text{Co}_3\text{O}_4/\text{Si}$ film shows the characteristic peaks of both Co_3O_4 and Si. The peaks at 1.06 and 2.06 V are related to the lithiation and delithiation process of Co_3O_4 , respectively [27]. The cathodic peaks, at 0.12 and 0.03 V, correspond to the typical multi-step lithiation process of Si, and the anodic peaks, at 0.36 and 0.50 V, are related to its reverse delithiation process [28, 29].

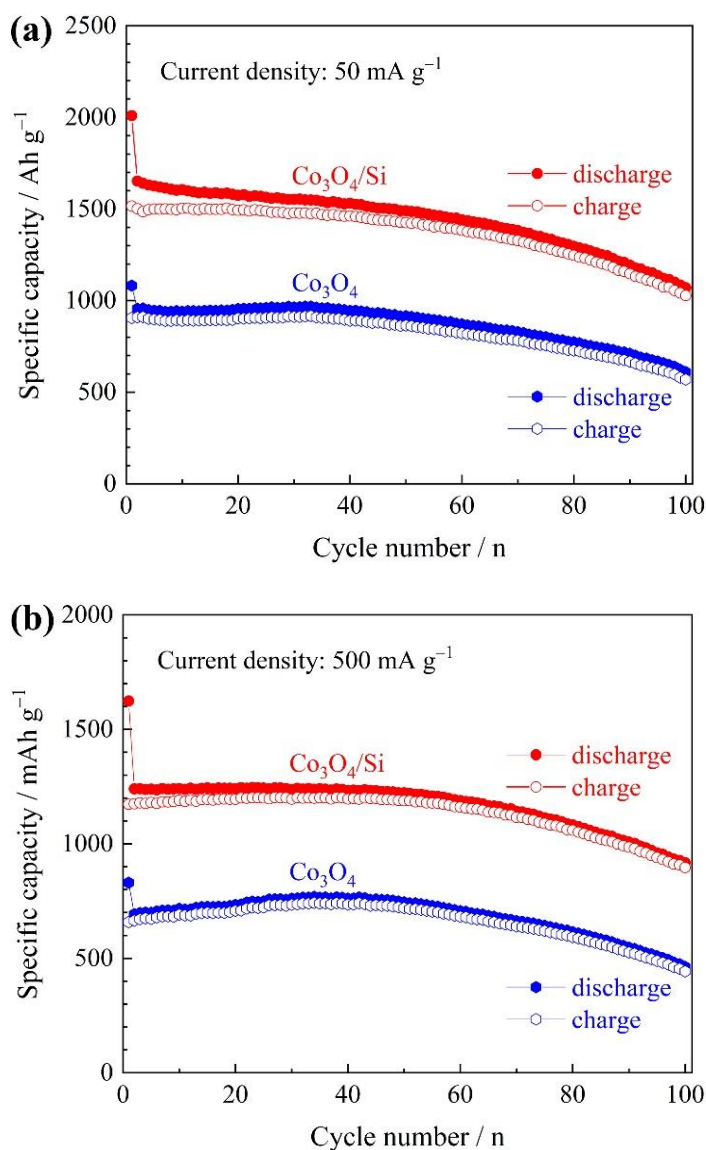


Figure 7. Cycling performances of the two film electrodes at (a) 50 mA g^{-1} and (b) 500 mA g^{-1} between 0.005 and 3 V.

To investigate the cycling stability and rate capability of the two samples, the electrodes are tested for 100 cycles at two different current densities of 50 and 500 mA g^{-1} . The evolution of their discharge and charge capacities during the cycling processes are compared in Figure 7. It is obvious that the $\text{Co}_3\text{O}_4/\text{Si}$ electrode delivers much higher capacity than the Co_3O_4 electrode during the whole cycling

process. At the low current density of 50 mA g^{-1} , the charge capacity of $\text{Co}_3\text{O}_4/\text{Si}$ electrode after 100 cycles is 1028 mAh g^{-1} , 68% of the initial value, and for Co_3O_4 electrode, these values are 569 mAh g^{-1} and 63%, respectively. When the current density increases to as high as 500 mA g^{-1} , the decrease in specific capacity of both materials is not significant, indicative of good rate capabilities. The 100th capacity of $\text{Co}_3\text{O}_4/\text{Si}$ is 897 mAh g^{-1} , 77% of the initial value, and for Co_3O_4 , they are 443 mAh g^{-1} and 67%, respectively. Therefore, it can be concluded that $\text{Co}_3\text{O}_4/\text{Si}$ composite film exhibits enhanced cycling performance compared with Co_3O_4 film. In addition, compared with other previously reported $\text{Co}_3\text{O}_4/\text{Si}$ composite, such as Co_3O_4 coated micro/nano-sized Si particles or nanowires, this interconnected $\text{Co}_3\text{O}_4/\text{Si}$ nanosheets also exhibit better electrochemical performance [30–32].

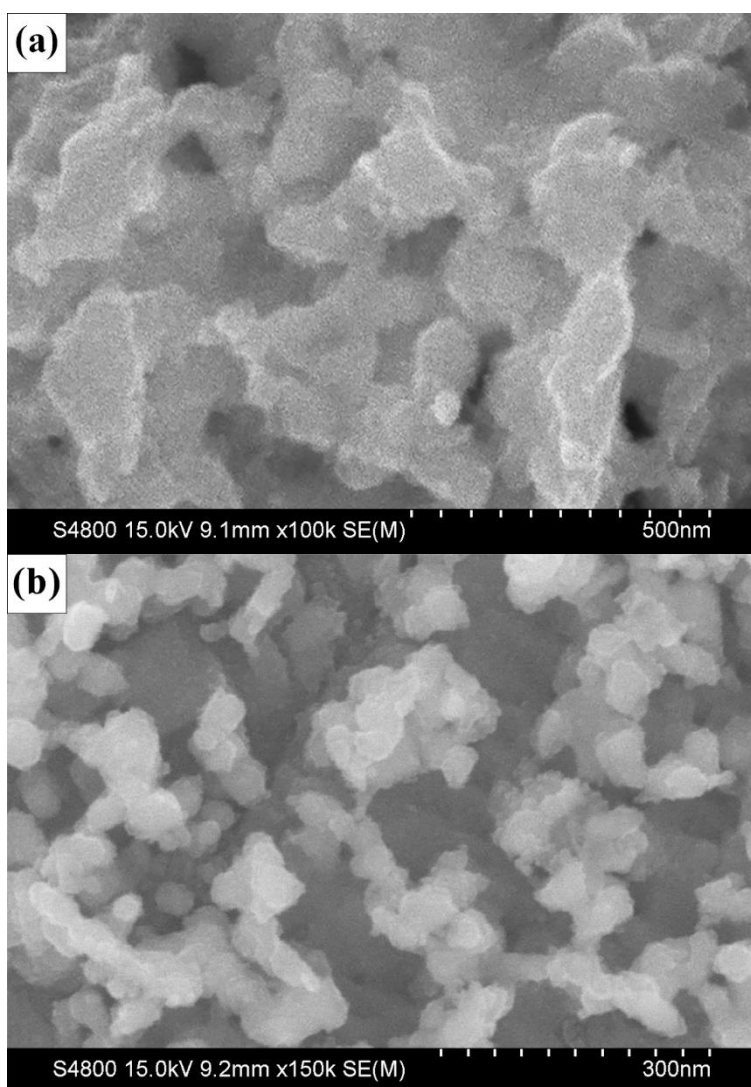


Figure 8. Comparison of SEM images of the (a) $\text{Co}_3\text{O}_4/\text{Si}$ and (b) Co_3O_4 films after cycling.

Structure stability of materials is a key factor for the cycling performance of electrodes. The morphology of the two film electrodes after cycling are characterized by SEM, as shown in Figure 8. For the $\text{Co}_3\text{O}_4/\text{Si}$ film electrode (Figure 8a), despite serious expansion and deformation of the nanosheets, part of the porous structure is still preserved. However, for the Co_3O_4 film, the original

porous interconnected network structure of is destroyed (Figure 8b). The ultrathin nanosheets changes into agglomeration of nanoparticles. Therefore, it can be concluded that the surface coating of Si on the nanosheets can enhance the stability of the interconnect network structure.

The enhanced electrochemical performance of the $\text{Co}_3\text{O}_4/\text{Si}$ film electrode is closely related to its composition and structure. The containing of Si component in the composite increases the overall specific capacity. The interconnected network structure is highly porous, and it has abilities of enlarging electrochemical reaction interface, shortening lithium-ion diffusion length, and buffering the volume expansion of active particles. Moreover, the Si coatings can reduce the pulverization of the nanosheets during the cycling process. These advantages lead to the reduction of electrode polarization and the enhancement of electrode structure stability, which are key factors for the rate capability and cycling performance.

4. CONCLUSIONS

In summary, $\text{Co}_3\text{O}_4/\text{Si}$ composite film has been successfully prepared on nickel foil substrate by chemical bath deposition in combination with magnetron sputtering. The film subjected to 20 min sputtering of Si has the best performance. This film has a porous network structure, constructed by interconnected $\text{Co}_3\text{O}_4/\text{Si}$ composite nanosheets, in which the areal densities of Co_3O_4 and Si are 0.15 and 0.16 mg cm^{-2} , respectively. Galvanostatic discharge-charge and cyclic voltammetry tests demonstrate the $\text{Co}_3\text{O}_4/\text{Si}$ composite film exhibits characteristic discharge/charge plateaus and cathodic/anodic peaks of both Co_3O_4 and Si. The comparison results of electrochemical performance show that this $\text{Co}_3\text{O}_4/\text{Si}$ composite film exhibits increased specific capacity and enhanced cycling performance as compared with the Co_3O_4 film. The Si component in the composite, the interconnected network structure of the film, and the Si-coated Co_3O_4 structure of the nanosheet play important roles in the enhancement of electrochemical performance.

ACKNOWLEDGMENTS

This work is supported by Zhejiang Provincial Natural Science Foundation of China (Grant Nos. LY16E020004 and LQ15E010001). We would like to acknowledge them for financial support.

References

1. P. Poizot, S. Laruelle, S. Grugeon, L. Dupont and J.M. Tarascon, *Nature*, 407 (2000) 496.
2. P. Poizot, S. Laruelle, S. Grugeon and J.M. Tarascon, *J. Electrochem. Soc.*, 149 (2002) A1212.
3. F. Zhang and L.M. Qi, *Adv. Sci.*, 3 (2016) 1600049.
4. X.H. Huang, J.P. Tu, Z.Y. Zeng, J.Y. Xiang and X.B. Zhao, *J. Electrochem. Soc.*, 155 (2008) A438.
5. H. Gao, H. Sun, A. Zhao, L. Wang and N. Liu, *Int. J. Electrochem. Sci.*, 13 (2018) 8666.
6. K.Q. Zhou, L.F. Lai, Y.C. Zhen, Z.S. Hong, J.H. Guo and Z.G. Huang, *Chem. Eng. J.*, 316 (2017) 137.
7. X.H. Huang, J.B. Wu, Y.Q. Cao, P. Zhang, Y. Lin and R.Q. Guo, *Electrochim. Acta*, 203 (2016) 213.

8. W.H. Liu, R.Y. Jin, Y.L. Li, Y.Y. Wu, X. Cao and S.Q. Hu, *Int. J. Electrochem. Sci.*, 13 (2018) 9520.
9. H. Li, X. Huang, L. Chen, Z. Wu and Y. Liang, *Electrochem. Solid-State Lett.*, 2 (1999) 547.
10. H. Wu and Y. Cui, *Nano Today*, 7 (2012) 414.
11. M.T. McDowell, S.W. Lee, W.D. Nix and Y. Cui, *Adv. Mater.*, 25 (2013) 4966.
12. Q.T. Wang, L.J. Han, X. Zhang, J. Li, X.Z. Zhou and Z.Q. Lei, *Mater. Lett.*, 185 (2015) 558.
13. T. Shen, Z.J. Yao, X.H. Xia, X.L. Wang, C.D. Gu and J.P. Tu, *Adv. Eng. Mater.*, 20 (2018) 1700591.
14. Y. Jin, B. Zhu, Z.D. Lu, N. Liu and J. Zhu, *Adv. Energy Mater.*, 7 (2017) 1700715.
15. Y.F. Chen, N. Du, H. Zhang and D.R. Yang, *J. Alloys Compd.*, 622 (2015) 966.
16. T. Huang, D.Y. Sun, W.X. Yang, H.L. Wang, Q. Wu and R.S. Xiao, *Scripta Mater.*, 146 (2018) 304.
17. H. Tang, Y.J. Zhang, Q.Q. Xiong, J.D. Cheng, Q. Zhang, X.L. Wang, C.D. Gu and J.P. Tu, *Electrochim. Acta*, 156 (2015) 86.
18. H.H. Zhang, X.H. Li, H.J. Guo, Z.X. Wang and Y. Zhou, *Powder Technol.*, 299 (2016) 178.
19. H. Wang, P. Wu, H.M. Shi, F.J. Lou, Y.W. Tang, T.G. Zhou, Y.M. Zhou and T.H. Lu, *Mater. Res. Bull.*, 55 (2014) 71.
20. X.W. Cheng, D.L. Zhao, L.L. Wu, Z.W. Ding, T. Hu and S. Meng, *Electrochim. Acta*, 265 (2018) 348.
21. K. Feng, M. Li, W.W. Liu, A.G. Kashkooli, X.C. Xiao, M. Cai and Z.W. Chen, *Small*, 14 (2018) 1702737.
22. M. Wu, N. Du, H. Wu, W. Liu, Y.F. Chen, W.J. Zhao and D.R. Yang, *Energy Technol.*, 4 (2016) 1435.
23. K.N. Shang, W.T. Li, Y.M. Liu, W.G. Zhang, H. Yang, J.Q. Xie, Z.Y. Liu, S.L. Chou, L.Z. Zhao and R.H. Zeng, *RSC Adv.*, 5 (2015) 70527.
24. Q.Q. Xiong, X.H. Xia, J.P. Tu, J. Chen, Y.Q. Zhang, D. Zhou, C.D. Gu and X.L. Wang, *J. Power Sources*, 240 (2013) 344.
25. D. Zhu, F. Zheng, S. Xu, Y. Zhang and Q. Chen, *Dalton Trans.*, 44 (2015) 16946.
26. D.Z. Kong, J.S. Luo, Y.L. Wang, W.N. Ren, T. Yu, Y.S. Luo, Y.P. Yang and C.W. Cheng, *Adv. Funct. Mater.*, 24 (2014) 3815.
27. X. Zhai, X. Xu, X. Zhu, Y. Zhao, J. Li and H. Jin, *J. Mater. Sci.*, 53 (2018) 1356.
28. H. Tang, J. Zhang, Y.J. Zhang, Q.Q. Xiong, Y.Y. Tong, Y. Li, X.L. Wang XL, C.D. Gu and J.P. Tu, *J. Power Sources*, 286 (2015) 431.
29. M.L. Jiao, J. Qi, Z.Q. Shi and C.Y. Wang, *J. Mater. Sci.*, 53 (2018) 2149.
30. Y.M. Kang, S.M. Lee, M.S. Sung, G.J. Jeong, J.S. Kim and S.S. Kim, *Electrochim. Acta*, 52 (2006) 450.
31. Y. Hwa, W.S. Kim, B.C. Yu, S.H. Hong and H.J. Sohn, *J. Phys. Chem. C*, 117 (2013) 7013.
32. F. Sun, K. Huang, Y.P. Liu, T. Tao, Y.N. Han and J.X. Zhong, *Appl. Surf. Sci.*, 266 (2013) 300.